Estimating Travel Time in Bank Filtration Systems from a Numerical Model Based on DTS Measurements

des Tombe, Bas F.; Bakker, Mark; Schaars, Frans; van der Made, Kees Jan

DOI
10.1111/gwat.12581

Publication date
2018

Document Version
Final published version

Published in
Groundwater

Citation (APA)
des Tombe, B. F., Bakker, M., Schaars, F., & van der Made, K. J. (2018). Estimating Travel Time in Bank Filtration Systems from a Numerical Model Based on DTS Measurements. *Groundwater*, *56*(2), 288-299. https://doi.org/10.1111/gwat.12581

Groundwater

Estimating Travel Time in Bank Filtration Systems from a Numerical Model Based on DTS Measurements

by Bas F. des Tombe[1], Mark Bakker[2], Frans Schaars[3], and Kees-Jan van der Made[4]

Abstract

An approach is presented to determine the seasonal variations in travel time in a bank filtration system using a passive heat tracer test. The temperature in the aquifer varies seasonally because of temperature variations of the infiltrating surface water and at the soil surface. Temperature was measured with distributed temperature sensing along fiber optic cables that were inserted vertically into the aquifer with direct push equipment. The approach was applied to a bank filtration system consisting of a sequence of alternating, elongated recharge basins and rows of recovery wells. A SEAWAT model was developed to simulate coupled flow and heat transport. The model of a two-dimensional vertical cross section is able to simulate the temperature of the water at the well and the measured vertical temperature profiles reasonably well. MODPATH was used to compute flowpaths and the travel time distribution. At the study site, temporal variation of the pumping discharge was the dominant factor influencing the travel time distribution. For an equivalent system with a constant pumping rate, variations in the travel time distribution are caused by variations in the temperature-dependent viscosity. As a result, travel times increase in the winter, when a larger fraction of the water travels through the warmer, lower part of the aquifer, and decrease in the summer, when the upper part of the aquifer is warmer.

Introduction

A bank filtration system is a type of managed aquifer recharge system where infiltration of water is induced at the bank of a water body and recovered by wells (e.g., Maliva and Missimer 2012). It is a cost-effective and sustainable filtration method for the production of potable water (Ray et al. 2003; Huelshoff et al. 2009; Maliva and Missimer 2012). The travel time during soil passage is a critical design parameter of a bank filtration system and needs to be large enough to result in, for example, pathogen-safe water (Schijven et al. 2003; Toze et al. 2010). Although tracer experiments have been used to determine the travel time from one observation well to another, it is practically very difficult to use them to determine the travel time distribution of a bank filtration system (Zheng et al. 2011; Ma et al. 2012). In this study, it is demonstrated how the travel time distribution can be derived from a passive heat tracer experiment. There are a variety of other methods that can be used to determine travel times in subsurface systems, see, for example, the recent summary by de Dreuzy and Ginn (2016).

In recent years, the use of heat as a tracer has increased due to the wide availability of temperature loggers and improved computer codes (Anderson 2005). The application of distributed temperature sensing (DTS) in hydrology made it possible to measure temperature along long fiber optic cables with a fine spatial resolution in a practical manner (e.g., Selker et al. 2006; Westhoff et al. 2007; Tyler et al. 2009; Steele-Dunne et al. 2010; Becker et al. 2013). Fiber optic cables have been lowered in boreholes to measure temperature variations, for example, to determine the terrestrial heat flow (e.g., Hurtig et al. 1993; Förster et al. 1997; Henninges et al. 2005) or local groundwater flow velocities and heat

[1]Corresponding author: Water Resources Engineering Section, Faculty of Civil Engineering and Geosciences, Delft University of Technology, Stevinweg 1, 2600 GA Delft, Netherlands; b.f.destombe@tudelft.nl

[2]Water Resources Engineering Section, Faculty of Civil Engineering and Geosciences, Delft University of Technology, Delft, Netherlands.

[3]Artesia, Schoonhoven, Netherlands.

[4]Wiertsema & Partners, Tolbert, Netherlands.

Article impact statement: Passive heat tracer experiment with DTS measurements and numerical modeling may be used to estimate travel times in Bank Filtration Systems.

Received December 2016, accepted July 2017.

doi: 10.1111/gwat.12581

transport (e.g., Read et al. 2013; Coleman et al. 2015). Estimation of aquifer thermal parameters using boreholes depends on the borehole thermal properties and the location of the heat source and temperature sensor within the borehole (Lembcke et al. 2015). Alternatively, fiber optic cables may be inserted into unconsolidated aquifers using direct-push equipment, so that no borehole is needed (Bakker et al. 2015).

Two types of heat tracer experiments may be distinguished: (1) active tracer experiments, where the water is actively heated and the response is measured (e.g., Leaf et al. 2012; Wagner et al. 2014; Bakker et al. 2015); and (2) passive heat tracer experiments, where groundwater temperature changes are caused by natural fluctuations in temperature (e.g., Anderson 2005; Hoehn and Cirpka 2006; Constantz 2008; Saar 2011). Passive heat tracer experiments usually cover a larger area than active heat tracer experiments and are well suited to determine the travel time distribution in bank filtration systems, provided the natural temperature fluctuations are large enough. The temperature of the groundwater in bank filtration systems is influenced by the temperature variations of the infiltrating water and the temperature variations at the soil surface, which may vary significantly throughout the year (e.g., Molina-Giraldo et al. 2011). Measured temperature profiles may be simulated with numerical models for coupled groundwater flow and heat transport. When such models are used for seasonally varying temperature conditions, they need to include the effect of the temperature of the groundwater on the flow field via the temperature-dependent viscosity.

The main objective of this study is to derive the variation in the monthly travel time distribution of water in a bank filtration system from a passive heat tracer experiment using a numerical model and DTS measurements. The temperature variation with depth is measured along vertically inserted fiber optic cables with a DTS system using the procedure developed by Bakker et al. (2015). The measured temperature variations are simulated in a two-dimensional (2D) vertical cross section with the coupled flow and heat transport code SEAWAT (Thorne et al. 2006). The numerical model is used to determine the variation of the monthly travel time distribution of the water. The second objective of this study is to determine the effect of variations in viscosity caused by temperature changes on the travel time distribution. The proposed approach is applied to a study site in the Netherlands.

Study Site

The study site is located in the dunes on the west coast of the Netherlands (Figure 1), where the drinking water company Provinciaal Waterleidingbedrijf Noord-Holland (PWN) operates a bank filtration system that produced 88 million cubic meters of potable water in 2014. In addition to filtration, the system serves as a back-up storage for when no water is available for infiltration, and to level out fluctuations in water quality. The system is also called a "Managed Aquifer Recharge system" or a "Dune Filtration System." The system is designed such that the travel time in the aquifer is at least 40 d. It consists of 12 parallel elongated shallow recharge basins to infiltrate pretreated river water and 682 shallow wells to recapture the water. The recharge basins are 20 to 40 m wide, several hundred meters long, and 1 to 2 m deep. Rows of wells are located between the basins. The well screens extend from 2.5 to 10 m below surface level. The wells are spaced 10 m apart and are connected via collection pipes to vacuum pumps with a controllable flow rate. The row of pumping wells is located in the middle between two recharge basins. The distance from the row of wells to either of the two banks is approximately 70 m (Figure 1). Recharge due to precipitation is approximately 1 mm/d. The flow rate (continuously), water temperature (continuously), and water quality (daily) are measured in the pumping station. In case pathogens are detected in the extracted water, wells continue to extract water to clean the system, but the water is routed back to the recharge basin ("Return Flow Outlet" in Figure 1), rather than to the treatment plant.

A schematic cross section along A–A′ (Figure 1) is shown in Figure 2. The aquifer is approximately 36 m thick, is subdivided into three sublayers, and is bounded at the bottom by a 10.5-m-thick clay layer. The first layer is 10.5 m thick and consists of coarse sand. The second layer is 12.5 m thick and consists of fine sand with thin clay layers. The third layer is 13 m thick and consists of coarse sand. Estimated saturated hydraulic conductivity values are presented in Figure 2 (PWN Sander de Haas, personal communication, 2014). Fiber optic cables were pushed 15 m into the ground at three locations using direct-push equipment (Bakker et al. 2015) and are labeled West, Center, and East. Fiber optic cables were connected in series using a Fujikura-FSM-70S fusion splicer (Fujikura Ltd., Tokyo, Japan), resulting in one long cable that was buried underground from the measurement locations to a nearby building with the DTS unit. There are two observation wells near the cross section. Observation well 1 is located near DTS-West (5.50 m below surface) and Observation well 2 (8.20 m below surface) is located in the gravel pack of a pumping well, three pumping wells (30 m) away from the cross section (Figure 2).

Measurements

The total discharge of the entire row of 45 wells is measured at the pumping station. The pumping rate is averaged per well and divided by 2, as approximately half the water comes from the recharge basin East of the rows of wells. The daily pumping rate (blue) and its 3-month moving average (black) are shown in Figure 3a. The return flow to the basin, when a pollution is detected in the extracted water, is indicated with the orange fill in Figure 3a.

The temperature is measured in Observation wells 1 and 2 and is shown in Figure 3b with green and purple lines, respectively. Although Observation well 2 is not located in the studied cross section A–A′, the measured temperature is expected to be representative for

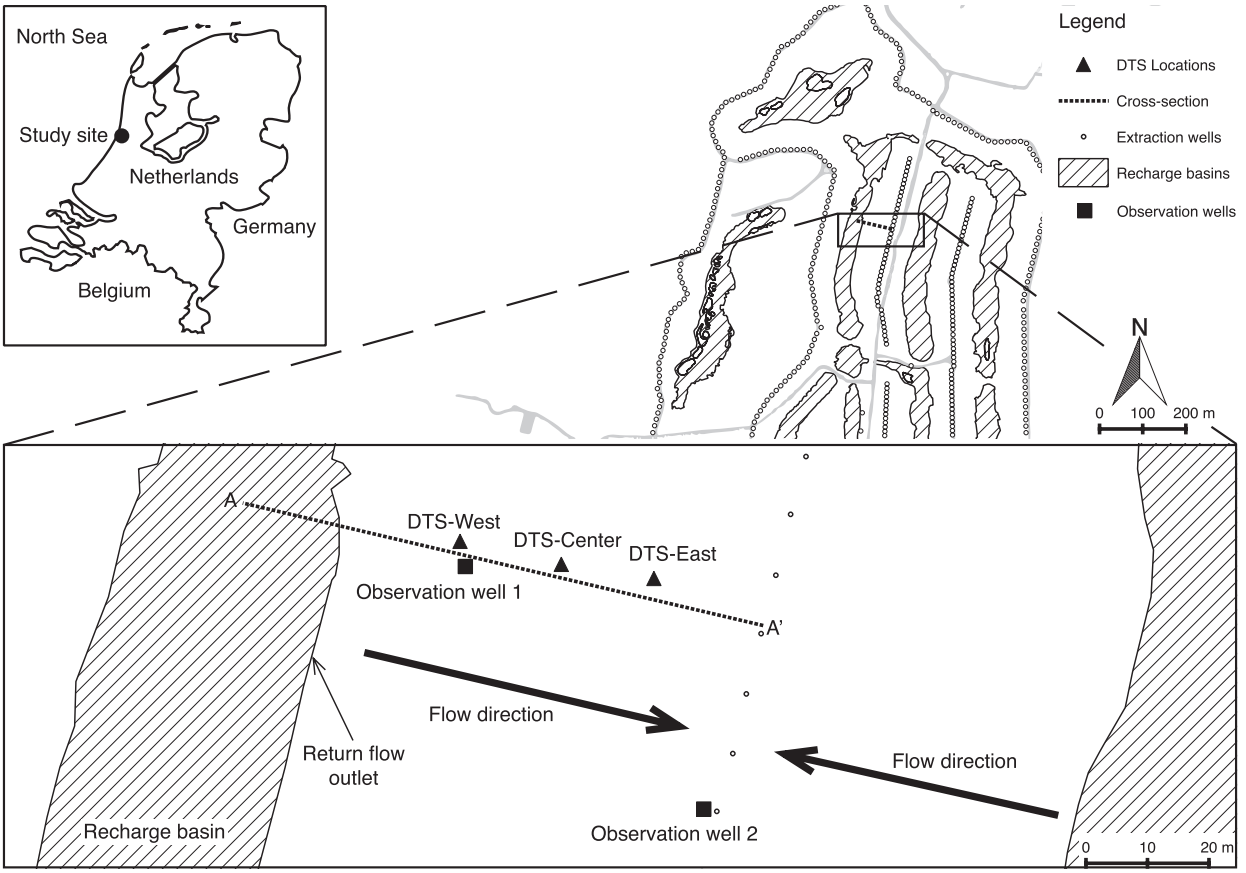

Figure 1. Map of the study site. Recharge basins (hatched), extraction wells (circles), DTS locations (triangles), and observation wells (squares). The WGS84 coordinates of the center DTS location are 4.6184° and 52.5514°.

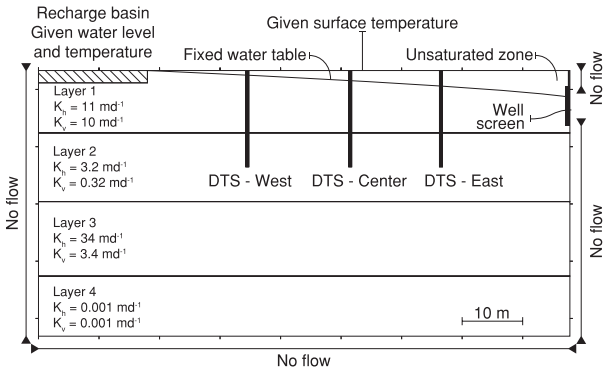

Figure 2. Schematic cross section of the aquifer along A–A′ in Figure 1, including flow boundaries for water and heat.

the same location in the cross section, as flow lines are approximately parallel to the cross section. A temperature sensor was placed at the bottom of the recharge basin. The last readout was in January 2014, after which the sensor failed. The measured time series is shown with a blue line in Figure 3b between "Start" and "End." Temperature measurements at 10 cm below ground surface at weather station De Bilt of the Royal Netherlands Meteorological Institute (located 63 km South East of the study site) show a remarkable resemblance with the available temperature measurements of the recharge basin and were used to fill the missing recharge basin temperature measurements (black line in Figure 3b). It is noted that this gap-filling is an approximation and does not take into account, for example, changes in the temperature of the recharge basin caused by the return flow in June, July, and October 2014. Temperature measurements at 5 cm below ground surface from the same weather station were used for the temperature at the ground surface of the study site (orange line in Figure 3b). The temperature signal at Observation wells 1 and 2 clearly differs in both the amplitude and the phase from the temperature signal in the recharge basin and at the ground surface.

Temperature profiles were measured along the fiber optic cable on April 24, June 3, August 7, and October 1 of 2014, and were averaged more than 24 h. The Silixa Ultima DTS system (Silixa Ltd., London, UK) was used for the first three measurement dates, providing a 0.13-m sample spacing. The Sensornet Oryx DTS system (Sensornet Ltd., Elstree, UK) was used for the measurements in October 2014, with a sample spacing of 1 m. The attenuation along the cable is corrected for by using the double-ended approach (van de Giesen et al. 2012) and cold and warm temperature baths were used for calibration. Four temperature profiles measured at location West are shown in Figure 4. The temperature at Observation well 1, located next to the DTS-West location, is plotted for validation of the DTS

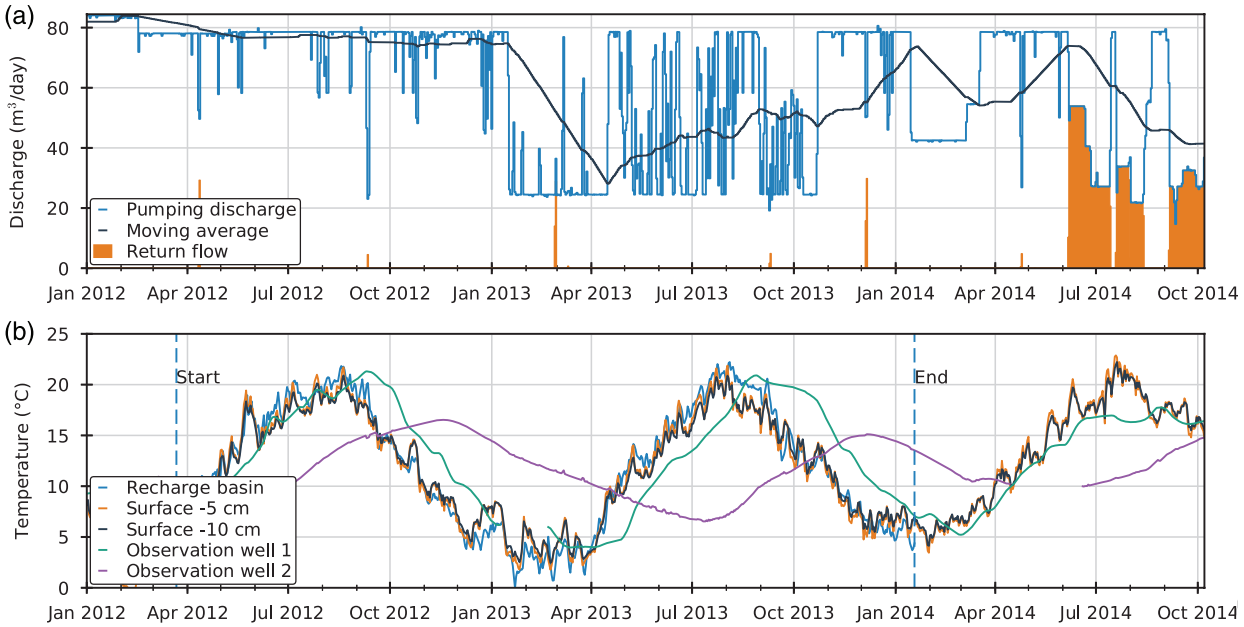

Figure 3. (a) Discharge of the pumping well (blue) divided by two, its 3-month moving average (black), and the discharge returned to the recharge basin upon detection of pollution (orange). (b) Temperature of the recharge basin (blue), measured between the "Start" and "End" labels, temperature at 5 cm and 10 cm below surface level (orange and black), and temperature in Observation wells 1 and 2 (green and purple).

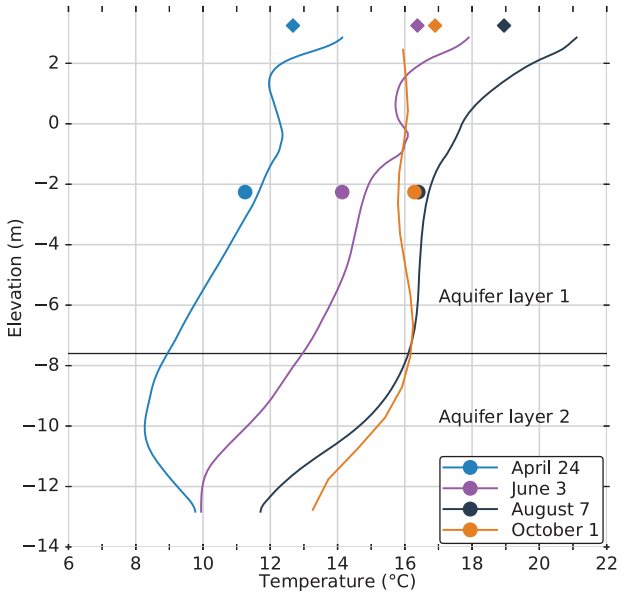

Figure 4. Temperature profile measured using DTS in 2014 at DTS-West location (lines), Observation well 1 temperature (dot), surface temperature (diamond).

measurements (dots). The measured temperature profiles match the temperature sensor measurements within 1 °C. The surface temperatures at −5 cm, measured at the weather station, are shown with diamonds. These are significantly lower than the DTS measurements, (up to 2 °C in August), except for October, when the −5 cm surface temperature is higher than the DTS measurement.

The vertical temperature profiles in the aquifer vary throughout the year. In April, the coolest water is present at −5 m, while the water is warmer above and below this depth. In June and August, the temperature decreases almost monotonically with depth, while in October the temperature increases with depth till −8 m after which it decreases. The largest temperature fluctuations are observed at the surface (7 °C more than the measurement period), while the temperature fluctuations at −13 m (layer 2, which has lower permeability) is only half the fluctuation at the surface (3.5 °C). In April, June, and August, the vertical temperature gradient near the surface indicates that heat is transported via conduction from the surface into the aquifer, while the reverse happens in October.

Mathematical Model

Heat transport in porous media is governed by thermal advection and thermal conduction. The heat transport equation may be written in a form analogous to the solute transport equation as (e.g., Thorne et al. 2006),

$$\frac{\partial T}{\partial t} = \nabla\left(\left[D^* + D\right]\nabla T\right) - \frac{1}{R}\nabla\left(\mathbf{u}T\right), \qquad (1)$$

where T is temperature [Θ], t is time [T], $\mathbf{u}$ is the groundwater velocity vector [LT^{-1}], D^* is the thermal diffusivity [L^{2}T^{-1}], D is the dispersion tensor [L^{2}T^{-1}], and R is the thermal retardation [−]. The latter three are related to the soil properties as,

$$D^* = \frac{k_b}{\rho_b c_b}, \quad D = \alpha\frac{\mathbf{u}}{R}, \quad R = \frac{\rho_b c_b}{\theta_w \rho_w c_w}, \qquad (2)$$

where ρ_b and ρ_w are the density of the bulk and water, respectively [ML^{-3}], θ_w is the water content [−], c_b and c_w are the specific heat capacity of the bulk and water, respectively [$L^2T^{-2}\Theta^{-1}$], k_b is the isotropic bulk thermal conductivity [$LMT^{-3}\Theta^{-1}$], and $\boldsymbol{\alpha}$ is the dispersivity tensor [L] with principal components α_L (longitudinal) and α_T (transverse). The water, solids, and air fractions are approximated as a single effective-medium of which the temperature is at instantaneous equilibrium.

The bulk density and bulk thermal capacity are calculated by the volume-weighted average of the properties of the moisture, air, and solids fractions (Nield and Bejan 2006),

$$\rho_b = \theta_s \rho_s + \theta_w \rho_w + \theta_a \rho_a, \quad c_b = \theta_s c_s + \theta_w c_w + \theta_a c_a, \tag{3}$$

where θ_s and θ_a are the volumetric fractions of the solids and air, respectively [−], ρ_s and ρ_a are the density of the solids and air, respectively [ML^{-3}], and c_s and c_a are the specific heat capacity of the solids and air, respectively [$L^2T^{-2}\Theta^{-1}$].

The bulk thermal conductivity depends on the pore structure (Nield and Bejan 2006; Wang and Pan 2008). Many averaging schemes exist, which either approximate the pore structure (e.g., series, parallel, EMI [Bruggeman 1935], Maxwell/Hashin & Shtrikman [Hashin and Shtrikman 1962]) or use empirical relations (e.g., Johansen 1977; Campbell 1985). Estimates for unsaturated soils are more difficult because of the large difference in thermal conductivity between the air and solid phase (Johansen 1977). The volume-weighted geometric mean is used here, which is suggested as a reasonable estimate (Johansen 1977; Nield and Bejan 2006),

$$k_b = k_s^{\theta_s} k_w^{\theta_w} k_a^{\theta_a}, \tag{4}$$

where k_s, k_w, k_a are the thermal conductances for solids, water, and air, respectively.

Groundwater flow is influenced by the temperature via viscosity and density. The hydraulic conductivity is defined as,

$$K_{sat} = \frac{\kappa \rho w g}{\mu}, \tag{5}$$

where K_{sat} is the saturated hydraulic conductivity [LT^{-1}], κ is the intrinsic permeability [L^2], μ is the dynamic viscosity [$ML^{-1}T^{-1}$], and g is the gravitational acceleration [LT^{-2}]. The relations between density and temperature (Langevin et al. 2008; Equation A5) and dynamic viscosity and temperature (Langevin et al. 2008; Equation 19) are approximated by,

$$\rho_w(T) = 999.1 - 0.1125 \cdot (T - 12), \tag{6}$$

$$\mu(T) = 10^{-3} \cdot \left[1 + 1.55 \cdot 10^{-2} \cdot (T - 20)\right]^{-1.572}, \tag{7}$$

where ρ_w is in kg/m^3, μ is in kg/m/s, and T is in °C. The groundwater temperature at the study site varies roughly between 4 and 20 °C. The corresponding variation in the water density is only 0.18%, but the viscosity varies with 36%, which results in a 57% higher hydraulic conductivity for water of 20 °C than for water of 4 °C.

The hydraulic conductivity, thermal conductivity, and heat capacity depend on the moisture content, each of which is lower in the unsaturated zone. This needs to be accounted for when modeling temperature signals in bank filtration systems (Molina-Giraldo et al. 2011). When vertical flow through the unsaturated zone is neglected, the moisture content above the water table may be calculated as (van Genuchten 1980),

$$S_e(h) = \frac{\theta_w(h) - \theta_{w,r}}{n - \theta_{w,r}} = \left[\frac{1}{1 + (\beta h)^{1/(2-m)}}\right]^m, \tag{8}$$

where S_e is the effective saturation [−], θ_w is the water content [−], $\theta_{w,r}$ is the residual soil-water content [−], n is the porosity [−], h is the height above the water table (cm), and β (cm^{-1}) and m (−) are soil-specific parameters. Values for medium grain-sized sand are used $\beta = 0.035$ cm^{-1}, $m = 0.67$ (Tuller and Or 2005). The hydraulic conductivity in the unsaturated zone is calculated with the van Genuchten's (1980) equation,

$$K_{unsat} = K_{sat} \sqrt{S_e} \left[1 - \left(1 - S_e^{1/m}\right)^m\right]^2 \tag{9}$$

Boundary Conditions

Two-dimensional groundwater flow and heat transport (Equation 1) are simulated in a vertical cross section (Figure 2) that is 10 m wide (the distance between two pumping wells). Total net precipitation on cross section A–A′ is approximately 1% of the mean pumping rate and is neglected. Flow in the direction normal to the cross section is neglected, including near the pumping well. Two rows of wells are positioned at an equal distance from each recharge basin (Figure 1), so that the vertical axis at the center of the recharge basin can be modeled as a no-flow boundary for water and heat. Two recharge basins are located at an approximately equal distance from the row of wells, so that the vertical boundary above and below the well screen can be modeled as a no-flow boundary for water and heat. The row of wells is modeled as a vertical line-sink with given uniform extraction rate. As stated, radial flow in the horizontal plane near the well is neglected. Vertical flow of water and heat at the bottom of the clay layer is neglected (no-flow boundary). The head and temperature are specified for the cells representing the recharge basin. The water level in the recharge basin is fixed to 2.92 m above mean sea level and the resistance of the leaky bed at the bottom of the recharge basin is set

to 1 d. The top boundary is a no-flow for groundwater and given temperature for heat transport. Estimates of the conductive and advective heat fluxes in the system are presented in Appendix, which shows that vertical advective heat transport is small compared to vertical conductive heat transport and horizontal advective heat transport. Vertical advective heat transport together with recharge is neglected at the top boundary.

Model Description

The coupled differential equations for the flow of heat and water are solved with the finite difference code SEAWAT (Langevin et al. 2008). Flow and heat transport are solved iteratively using the generalized conjugate gradient solver, where the thermal conduction is solved with an implicit finite difference scheme and the thermal convection is solved using a third-order total-variation-diminishing scheme with a stability constraint (Zheng and Wang 1999). The input files for SEAWAT were written and the output files were read using the open-source Python package FloPy (Bakker et al. 2016) in Jupyter notebooks.

The modeled cross section is 46 m deep, 88 m long, and 10 m wide. The cross section is discretized vertically into 107 model layers, with cells of 7.5 cm high near the surface (to account for the large temperature gradients) increasing to 1 m high for the lower part of the model. The cross section is discretized horizontally into 88 columns of 1 m long. The modeling period is from 2012 to 2014, with a spin-up period starting in 1988. All boundary conditions are specified on a daily basis and each day is split into 10 calculation steps to comply with the convergence criteria. The flow is modeled as transient, with the specific yield set to 0.25 for unsaturated cells and the storage coefficient for saturated cells set to $10^{-5}\,m^{-1}$. Values for the aquifer properties used in the SEAWAT model are presented in Table 1 and Figure 2. The recharge basin is modeled using the River package and the well using the Well package in SEAWAT.

No unsaturated packages currently exist for SEAWAT. Therefore, an approximate approach is used to model flow and heat transport through the unsaturated zone. First, the water table is calculated by averaging the head in the top cells of the last year of the spin-up period. Then the water table is used to calculate the thermal capacity, the thermal conductance, and the hydraulic conductivity in the unsaturated zone at reference temperature using Equations 3, 4, and 9, respectively.

The spin-up period starts in 1988 with a uniform temperature of 12 °C and a water table equal to the surface elevation. A yearly sine function is used for the temperature of the recharge basin and at the soil surface during spin-up (based on available temperature measurements). A constant discharge was of $60\,m^3/d$ is used during spin-up (average of the period 2010 to 2014). The spin-up period is split in two parts. In the first part, 1988 to 2007, the top of the model is horizontal and no unsaturated zone is modeled. The head in the top cells is averaged over the year 2007 and is used to compute the average position of the water table and to calculate unsaturated zone properties for the second part of the spin-up period from 2008 to 2011.

Table 1
Hydraulic and Thermal Aquifer Properties

ρ_s	Density of the solids	2710 kg/m^3
ρ_w	Density of the water (at 12 °C)	999.1 kg/m^3
ρ_a	Density of the air	1.2 kg/m^3
c_s	Specific heat capacity of solids	835 J/kg/°C
c_w	Specific heat capacity of water	4183 J/kg/°C
c_a	Specific heat capacity of air	1005 J/kg/°C
k_s	Thermal conductivity of solids	4.85 W/m/°C
k_w	Thermal conductivity of water	0.58 W/m/°C
k_a	Thermal conductivity of air	0.0257 W/m/°C
n	Porosity	0.35
S_s	Storage coefficient	$10^{-5}\,m^{-1}$
S_y	Specific yield	0.25
α_L	Longitudinal dispersivity	0.1 m
α_T	Transversal dispersivity	0.01 m

No formal calibration is conducted, for example, using a parameter estimation package such as PEST (Doherty 2016), because the temperature of the recharge basin and at the surface was not measured correctly during the entire experiment. Although reasonable substitutes are obtained (see Figure 3), it makes formal calibration an exercise on how aquifer and heat transport parameters can take on surrogate roles to compensate for errors in the input series.

The travel time of a water particle from the recharge basin to the extraction well is computed with MODPATH (Pollock 2012). MODPATH uses a continuous velocity field by linearly interpolating the velocities across cell boundaries calculated with SEAWAT. The porosity (Table 1) is used to calculate an average pore flow velocity. The cumulative flux along the cell faces representing the well screen is computed at the desired arrival time. One thousand particles are spaced such that each particle represents 0.1% of the extracted volume. The particles are released and tracked backward in time until they reach the recharge basin to compute the travel time for each of the one thousand particles.

Model Results

The measured temperature in Observation well 1 (blue) and Observation well 2 (orange) and their corresponding modeled temperatures (black and purple, respectively) are shown in Figure 5. The root-mean-square error (RMSE) between modeled and measured temperatures is 1.28 °C at Observation well 1 and 0.72 °C at Observation well 2. The amplitudes of the modeled temperature variations are in accordance with the amplitudes of the measured temperatures, with the largest differences for Observation well 1 in the winter months. The phase-shift and the timing of the modeled temperature peaks coincide with the measurements. The RMSE between the modeled

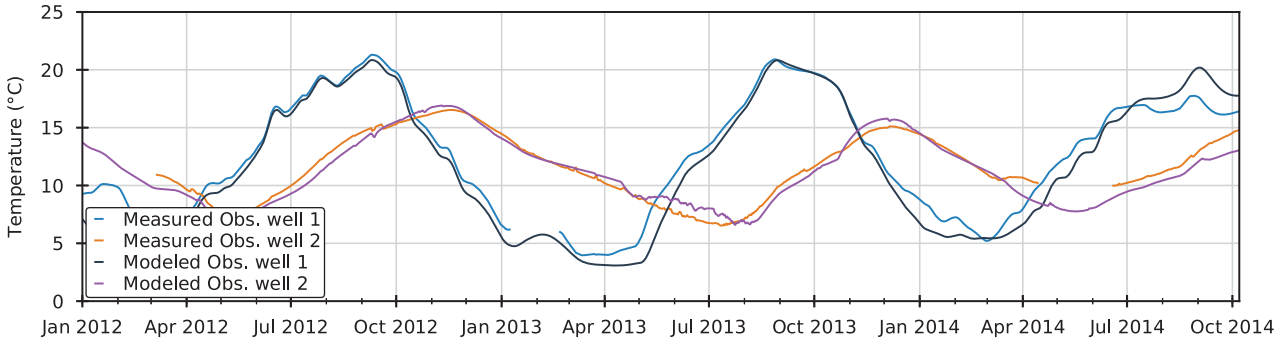

Figure 5. Measured and modeled temperature at Observation wells 1 and 2.

and measured heads at Observation well 1 is 0.49 m (not shown). Comparison of the modeled heads to measured heads at Observation well 2 is not meaningful, as radial flow in the horizontal direction is neglected.

Temperature measurements (blue) at the three DTS locations for the four measurement dates are compared to model results (orange) in Figure 6. The fixed water table is shown with the dashed line. The measured and simulated temperature profiles show similar behavior but also distinct differences. The RMSE between the modeled and measured temperature profiles is 1.81 °C. The lowest RMSE of (1.21 °C) is calculated for location East in October and the highest RMSE of (2.20 °C) is calculated for location West in June. The temperature transition from the approximate water table to the surface is visible in both the modeled and the measured temperature profiles. The bends in the temperature profiles just above the water table are matching well for April and October, 2014. The bend in the temperature profile of June 2014 is located higher in the model as compared to the measurement. At that time the actual water table is probably lower compared to other months due to high pumping rates, so that the bend in the measurements is at a lower elevation than in the model. In August, the specified temperature at the surface is 2 °C lower than the surface temperature measured with DTS (Figure 4), resulting in an offset between measured and simulated temperature in the upper part of the temperature profiles in August. Furthermore, a bend is missing in the upper half of the August measurement at location West. This is likely due to the effects of the return flow (orange fill in Figure 3), when all of the cold extracted water in June and July was returned to the recharge basin. These effects are not accounted for in the specified temperature of the recharge basin.

The travel time of the extracted water was calculated for each month between November 2013 and October 2014 and is shown in Figure 7. Note that the travel time, plotted on the vertical axis, is on log-scale. The color of the line represents the travel time for which xx% of the flow is faster and is referred to as the $t_{xx\%}$ line. The gray level of the fill represents the maximum depth reached by a water particle: the light-gray fill represents water particles that only moved through the first aquifer layer, the medium-gray fill represents water particles that reached the second aquifer layer, and the dark-gray fill represents water particles that reached the third aquifer layer. Water particles that reach the third aquifer layer take at least 500 d to travel from the recharge basin to the extraction well. The bottom graph shows the corresponding monthly discharge of the pumping well. The $t_{50\%}$ line varies significantly from month to month and is strongly related to the pumping discharge (when the discharge is high, $t_{50\%}$ is low). The shortest travel times are less than 40 d and occur in the months with the highest discharge.

Travel Time Variation under Constant Pumping

An additional simulation was performed with a constant discharge and a sinusoidal variation of the temperature in the recharge basin and at the surface to isolate the effect of a seasonal temperature variation on the flow. An illustrative figure of the approximate instantaneous streamlines is shown in Figure 8; the discharge is the same between any two adjacent streamlines. The largest fraction of the water flows through the first aquifer layer. The placement of the recharge basin at the top of the aquifer and the extraction well near the top of the aquifer result in curvature of the groundwater streamlines and pathlines. The flow velocities in the second aquifer layer are low, with a vertical velocity component pointing downward at DTS-West and upward at DTS-East.

The variation of the travel time from month to month at the study site is strongly affected by the variation in the discharge of the wells (Figure 7). The effect of seasonal temperature variations on the travel time distribution in the simulation with a constant discharge and a sinusoidal variation of the temperature in the recharge basin and at the surface is shown in Figure 9. The figure contains two sets of lines. The dashed lines include solely the effects of varying density, while the continuous lines include both the effect of varying density and viscosity. The influence of density variations on the travel time distribution is negligible, as stated, resulting in virtually the same travel times for each month. The influence of a varying viscosity on the travel time distribution is significant. For constant viscosity, the $t_{10\%}$ is constant and equal to 45 d throughout the year, while a varying viscosity results in a variation

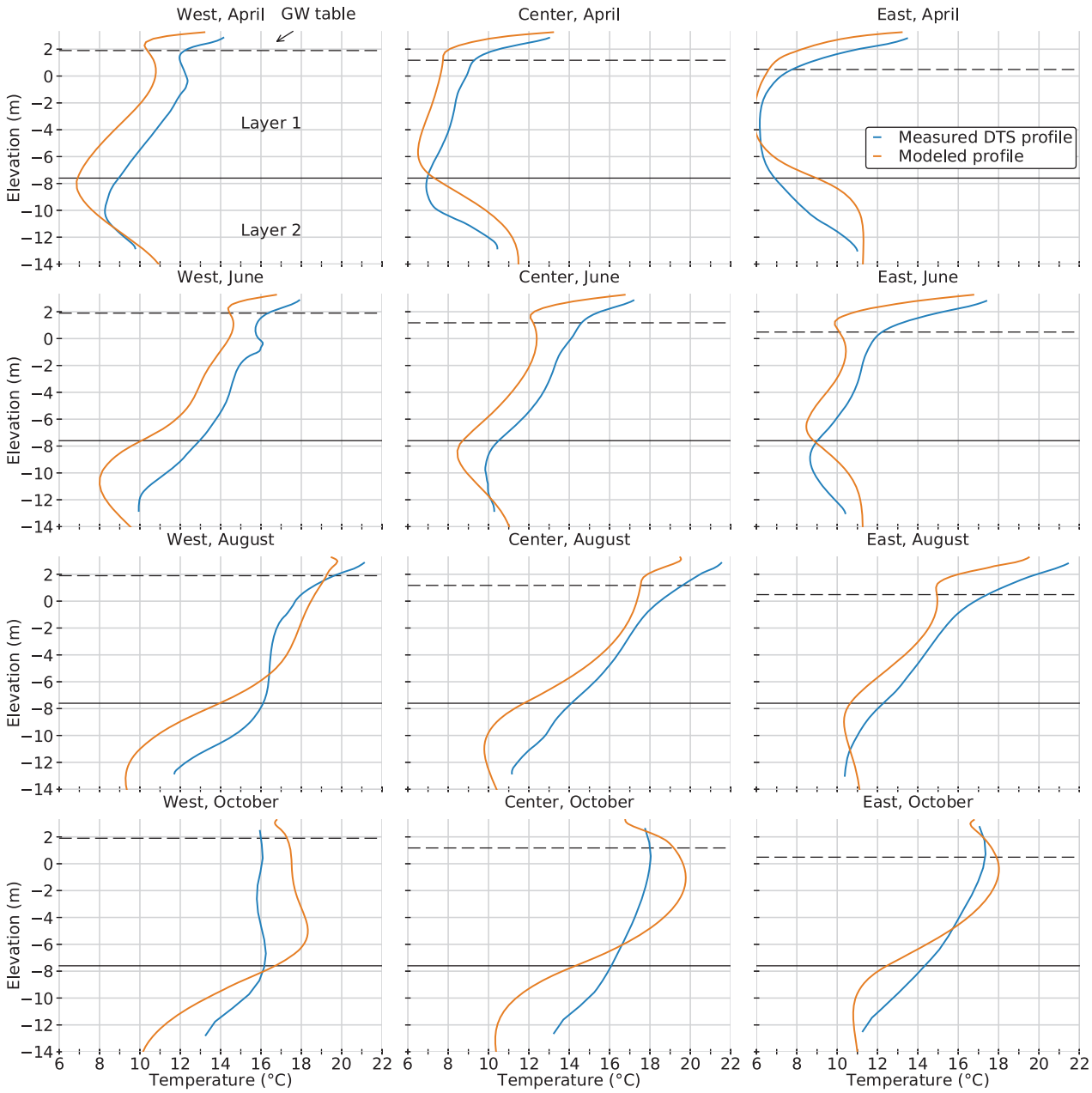

Figure 6. Measured DTS temperature (blue) and modeled temperature (orange), fixed water table in model (black dashed line), and interface between aquifer layer 1 and aquifer layer 2 (black solid line).

from 42 d in the warmest period (August) to 49 d in the coldest period (February). The $t_{75\%}$ line shows a much larger range, varying from 64 to 195 d, while the travel time for constant viscosity is 119 d.

The cumulative flow is computed in the aquifer at section B–B′ (Figure 8) and is shown in Figure 10. In February, 30% of the water flows through the second and third aquifer layer, while it is 24% (so 20% less) in August. Water that travels via the second and third aquifer layer moves a lot slower, as can be seen from the distance between the streamlines shown in Figure 8. This seasonal difference results in the large variation of the $t_{75\%}$ line in Figure 9.

Discussion

Temperature measurements of the water in the recharge basin and at the soil surface are essential for the simulation of flow and heat transport in the system. These measurements were not available for the period of the experiment at the study site. Surface temperatures from weather station De Bilt were used as reasonable substitutes. Aquifer parameters at the study site have been studied for several decades by the drinking water company that operates the bank filtration system, so that reasonable estimates were available.

A separate model was constructed to determine the importance of heat conduction from the top boundary. The top model boundary for heat flow was simulated

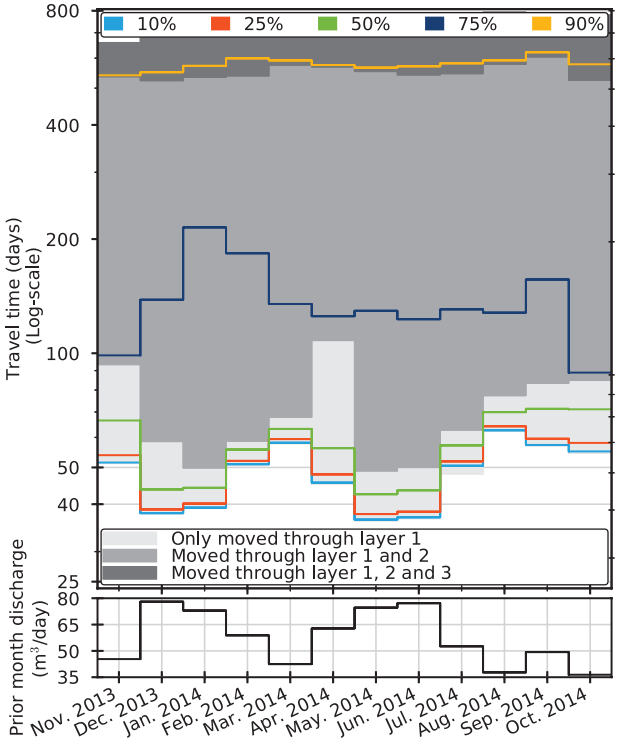

Figure 7. Upper: travel time distribution per month. The distribution of the travel time is plotted with the colored lines. Note that the vertical axis is log-scaled. Lower: monthly average discharge of the prior month.

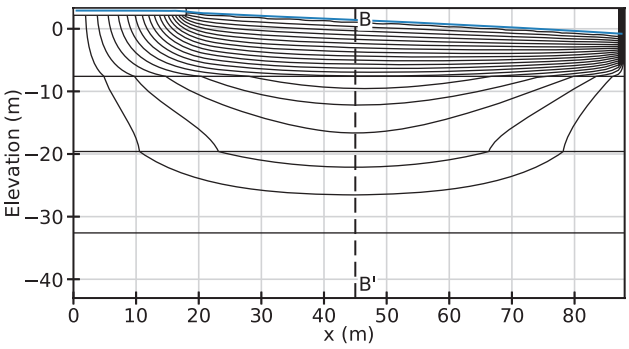

Figure 8. Modeled instantaneous streamlines in the vertical cross section at the study site.

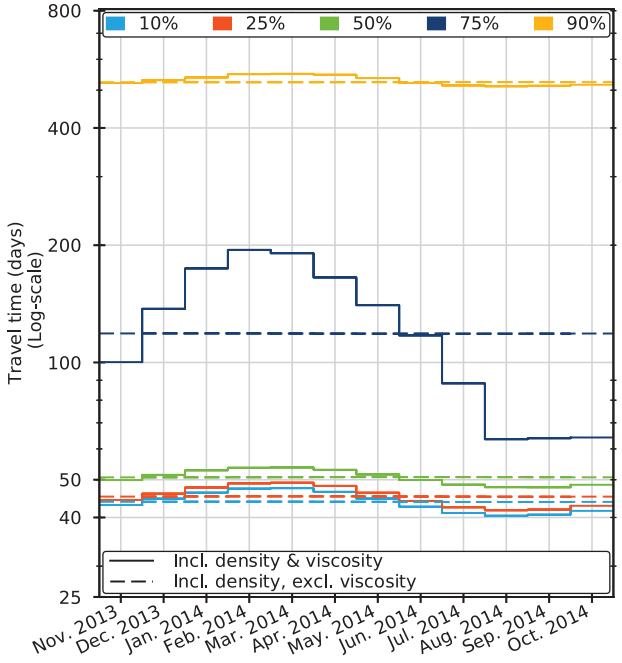

Figure 9. Travel time distribution with constant discharge and a sinusoidal surface and recharge basin temperature.

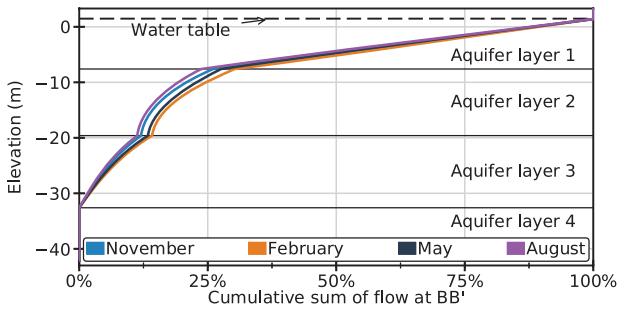

Figure 10. The modeled cumulative sum of the flow along section B-B′ (Figure 8) under constant pumping, on the 15th of the month.

as isolating instead of a given temperature. This model showed a similar temperature response at Observation well 2 as the model with a given temperature along the top boundary, but the vertical temperature profiles differed significantly near the top of the model, where they are normal to the isolating top boundary. Travel time distributions were also calculated for this modified model and did not differ much from the scenario with a given surface temperature.

The temperature boundary at the bottom is approximated with an isolating boundary. If this boundary is deep enough, the temperature variation along the bottom should be negligible. The maximum temperature variation over 2013 to 2014 is 0.34 °C at the bottom of the model below the recharge basin, 0.27 °C in the center of the bottom and 0.06 °C at the bottom below the well. These variations are small compared to the temperature variation at the surface, which means that the placement of the bottom boundary is deep enough.

Radial flow in the horizontal plane near the well is neglected. The consequences of this approximation are estimated by calculating the travel time in a 1D situation and comparing it to the travel time in a 2D horizontal situation. The travel time is at most 2.6% shorter when modeled as 2D flow than when modeled as 1D flow but approximately 15% of the flow has significantly larger travel times. This means that neglecting radial flow is reasonable when estimating the shortest travel time but less reasonable when estimating the largest travel times. This is in line with the primary interest of the drinking water company, which is the fastest few percent of the flow.

Conclusions

A passive heat tracer experiment was conducted at a bank filtration system to estimate seasonal variations in the travel time distribution. The bank filtration system consists of recharge basins and rows of recovery wells. The temperature in the system varies throughout the year because of temperature variations of the recharge basin and at the surface. The temperature was measured at two observation wells regular temperature sensors. The temperature was also measured at three locations along vertically installed fiber optic cables using DTS. The main advantages of the latter method are that the fiber optic cables are in direct contact with the aquifer and are able to measure the temperature distribution along vertical lines in the aquifer.

A coupled flow and heat transport model was constructed with SEAWAT. As the model is able to simulate the measured temperature profiles and the measured temperature in the two observation wells, it can be used to compute the travel time distribution from the recharge basin to the wells. The discharge of the pumping wells varies significantly at the study site, which strongly affects the shortest travel times and overshadows the effect of temperature changes on the travel time distribution. The influence of seasonal temperature variations on the travel time distribution was examined by simulating flow in the system with a constant pumping discharge and approximating the temperature of the recharge basin and at the surface with a sinusoidal function with a period of 1 year. This model showed that viscosity changes caused by temperature changes resulted in a significant temporal variation of the travel time distribution. Arrival of the fastest 10% of the water varied between 42 and 49 d. In the winter, a larger portion of the water flows through the deeper, less permeable aquifer layer, when the water in that layer is warmer as compared to the water in the top aquifer layer. As a result, arrival of the fastest 75% of the water varied between 64 and 195 d.

In conclusion, a passive heat tracer experiment consisting of DTS measurements of temperature along vertically installed fiber optic cables combined with numerical modeling of flow and heat transport is a promising approach to estimate travel time distributions in bank filtration systems. Seasonally varying viscosity needs to be taken into account in the design of the maximum pumping rate for bank filtration systems, especially when the pumping discharge is relatively constant. Operators need to be aware that the risk of pathogen contamination may increase in the summer months because of shorter travel times, which may warrant lower pumping rates.

Acknowledgments

This work was funded in part by the Netherlands Organization for Scientific Research (NWO), program The New Delta with project number 869.15.006. The authors thank Sander de Haas, Ed Rasenberg, and Lucas Borst for hosting the study site at PWN, Ruben Caljé (Artesia, NL) for his assistance with the DTS equipment and analyzing the temperature measurements, and Koen Hilgersom (TU Delft, NL) for assistance with the splicing of the fiber optic cables. The constructive suggestions of the Associate Editor, Grant Ferguson, and two anonymous reviewers helped improve this paper.

Appendix

Estimation of Advective and Conductive Heat Fluxes

The order of magnitude of the advective heat transport and conductive heat transport are estimated for the 2D vertical cross section on a yearly timescale. The advective heat flux F [MLT^{-3}] and the conductive heat flux G [MLT^{-3}] in the horizontal (x) and vertical (z) direction are given by,

$$F_x = \rho_w c_w q_x H \frac{\partial T}{\partial x} \tag{A1}$$

$$F_z = \rho_w c_w q_z L \frac{\partial T}{\partial z} \tag{A2}$$

$$G_x = k_b H \frac{\partial T}{\partial x} \tag{A3}$$

$$G_z = k_b L \frac{\partial T}{\partial z} \tag{A4}$$

where H refers to the height of the aquifer [L], L to the distance between the recharge basin and the extraction well [L], and q to the specific discharge [LT^{-1}]. The temperature gradients are approximated following (e.g., Van Der Kamp and Bachu 1987; Anderson 2005),

$$\frac{\partial T}{\partial x} \approx \frac{[\Delta T]_x}{L} \tag{A5}$$

$$\frac{\partial T}{\partial z} \approx \frac{[\Delta T]_z}{H} \tag{A6}$$

where $[\Delta T]_x$ is the temperature difference between the recharge basin and at the extraction well [Θ] and $[\Delta T]_z$ is the temperature difference between the surface and the bottom of the aquifer [Θ].

Representative values for the studied bank filtration system are, $q_x = 0.42$ m/d, $q_z = 1$ mm/d, $L = 70$ m, $k_b = 2.3$ W/m/°C, $H = 10$ m, $[\Delta T]_x = 4.8$ °C, and $[\Delta T]_z = 10$ °C, which results in the following,

$$F_x = 980 \text{ W/m}$$

$$F_z = 34 \text{ W/m}$$

$$G_x = 1.6 \text{ W/m}$$

$$G_z = 160 \text{ W/m}$$

The advective heat flux due to areal recharge (F_z) is much smaller than the horizontal advective heat flux (F_x)

and the vertical conductive heat flux (G_x). The advective heat flux due to areal recharge can therefore safely be neglected.

References

Anderson, M.P. 2005. Heat as a ground water tracer. *Groundwater* 43, no. 6: 951–968.

Bakker, M., V. Post, C.D. Langevin, J.D. Hughes, J.T. White, J.J. Starn, and M.N. Fienen. 2016. Scripting MODFLOW model development Using Python and FloPy. *Groundwater* 54: 733–739. https://doi.org/10.1111/gwat.12413.

Bakker, M., R. Caljé, F. Schaars, K.-J. van der Made, and S. de Haas. 2015. An active heat tracer experiment to determine groundwater velocities using fiber optic cables installed with direct push equipment. *Water Resources Research* 51, no. 4: 2760–2772.

Becker, M.W., B. Bauer, and A. Hutchinson. 2013. Measuring artificial recharge with fiber optic distributed temperature sensing. *Groundwater* 51, no. 5: 670–678.

Bruggeman, D.A.G. 1935. Berechnung verschiedener physikalischer Konstanten von heterogenen Substanzen. I. Dielektrizitätskonstanten und Leitfähigkeiten der Mischkörper aus isotropen Substanzen. *Annalen der Physik* 416, no. 7: 636–664.

Campbell, G. 1985. *Soil Physics with BASIC: Transport Models for Soil-Plant Systems. Developments in Soil Science*. Amsterdam: Elsevier Science.

Coleman, T.I., B.L. Parker, C.H. Maldaner, and M.J. Mondanos. 2015. Groundwater flow characterization in a fractured bedrock aquifer using active DTS tests in sealed boreholes. *Journal of Hydrology* 528: 449–462.

Constantz, J. 2008. Heat as a tracer to determine streambed water exchanges. *Water Resources Research* 44, W00D10. https://doi.org/10.1029/2008WR006996.

de Dreuzy, J.-R., and T. Ginn. 2016. Residence times in subsurface hydrological systems, introduction to the special issue. *Journal of Hydrology* 543, no. Part A: 1–6.

Doherty, J. 2016. *PEST, Model-Independent Parameter Estimation—User Manual*, *Watermark Numerical Computing*, 6th ed. Brisbane, Australia. pesthomepage.org.

Förster, A., F. Andrea, J. Schrötter, D.F. Merriam, and D.D. Blackwell. 1997. Application of optical fiber temperature logging: An example in a sedimentary environment. *Geophysics* 62, no. 4: 1107–1113.

Hashin, Z., and S. Shtrikman. 1962. A variational approach to the theory of the effective magnetic permeability of multiphase materials. *Journal of Applied Physics* 33, no. 10: 3125–3131.

Henninges, J., Zimmermann, G., Büttner, G., Schrötter, J., Erbas, K., and Huenges, E. 2005. Wireline distributed temperature measurements and permanent installations behind casing. In *Proceedings of the World Geothermal Congress 2005*, Antalya, Turkey, ed. R. Horne and E. Okandan.

Hoehn, E., and O.A. Cirpka. 2006. Assessing residence times of hyporheic ground water in two alluvial flood plains of the southern alps using water temperature and tracers. *Hydrology and Earth System Sciences* 10, no. 4: 553–563.

Huelshoff, I., J. Greskowiak, and G. Gruetzmacher. 2009. Chapter 5.2.3: Analysis of the vulnerability of bank filtration systems to climate change by comparing their effectiveness under varying environmental conditions. In *Combination of MAR and Adjusted Conventional Treatment Processes for an Integrated Water Resources Management*, ed. Y.M. LeGolvan, J. Burgschweiger, and P. Stuyvzand. Techneau.

Hurtig, E., J. Schrötter, S. Großwig, K. Kühn, B. Harjes, W. Wieferig, and R. Orrell. 1993. Borehole temperature measurements using distributed fibre optic sensing. *Scientific Drilling* 3, no. 6: 283–286.

Johansen, O. 1977. Thermal conductivity of soils. Ph.D. thesis, University of Trondheim.

Langevin, C.D., D.T. Thorne Jr., A.M. Dausman, M.C. Sukop, and W. Guo. 2008. SEAWAT Version 4: A Computer Program for Simulation of Multi-Species Solute and Heat Transport: U.S. Geological Survey Techniques and Methods Book 6, Chapter A22, 39 p.

Leaf, A.T., D.J. Hart, and J.M. Bahr. 2012. Active thermal tracer tests for improved hydrostratigraphic characterization. *Groundwater* 50, no. 5: 726–735.

Lembcke, L.G.M., D. Roubinet, J. Irving, B.L. Parker, and F. Gidel. 2015. Analytical analysis of borehole experiments for the estimation of subsurface thermal properties. *Advances in Water Resources* 91: 1–7.

Ma, R., C. Zheng, J.M. Zachara, and M. Tonkin. 2012. Utility of bromide and heat tracers for aquifer characterization affected by highly transient flow conditions. *Water Resources Research* 48, no. June: 1–18.

Maliva, R.G., and T.M. Missimer. 2012. Arid lands water evaluation and management. In *Environmental Science and Engineering*. *Environmental Science and Engineering*, chapter Managed Aq, Vol. 3, ed. R. Allan, U. Förstner, and W. Salomons, 806. Berlin/Heidelberg: Springer.

Molina-Giraldo, N., P. Bayer, P. Blum, and O.A. Cirpka. 2011. Propagation of seasonal temperature signals into an aquifer upon bank infiltration. *Groundwater* 49, no. 4: 491–502.

Nield, D.A., and A. Bejan. 2006. *Convection in Porous Media*. New York: Springer.

Pollock, D.W. 2012. User Guide for MODPATH Version 6—A Particle–Tracking Model for MODFLOW: U.S. Geological Survey Techniques and Methods 6-A41, 58 p.

Ray, C., J. Schubert, R.B. Linsky, and G. Melin. 2003. *Riverbank Filtration: Improving Source-Water Quality*. Dordrecht, Netherlands: Kluwer Academic Publishers.

Read, T., O. Bour, V. Bense, T.L. Borgne, P. Goderniaux, M.V. Klepikova, R. Hochreutener, N. Lavenant, and V. Boschero. 2013. Characterizing groundwater flow and heat transport in fractured rock using fiber-optic distributed temperature sensing. *Geophysical Research Letters* 40, no. 10: 2055–2059.

Saar, M.O. 2011. Review: Geothermal heat as a tracer of large-scale groundwater flow and as a means to determine permeability fields. *Hydrogeology Journal* 19, no. 1: 31–52.

Schijven, J., P. Berger, and I. Miettinen. 2003. *Removal of Pathogens, Surrogates, Indicators, and Toxins Using Riverbank Filtration*, 73–116. Dordrecht, Netherlands: Springer.

Selker, J.S., L. Thévenaz, H. Huwald, A. Mallet, W. Luxemburg, N. van de Giesen, M. Stejskal, J. Zeman, M. Westhoff, and M.B. Parlange. 2006. Distributed fiber-optic temperature sensing for hydrologic systems. *Water Resources Research* 42, W12202. https://doi.org/10.1029/2006WR005326.

Steele-Dunne, S.C., M.M. Rutten, D.M. Krzeminska, M. Hausner, S.W. Tyler, J. Selker, T.A. Bogaard, and N.C. van de Giesen. 2010. Feasibility of soil moisture estimation using passive distributed temperature sensing. *Water Resources Research* 46, no. 3: W03534.

Thorne, D., C.D. Langevin, and M.C. Sukop. 2006. Addition of simultaneous heat and solute transport and variable fluid viscosity to SEAWAT. *Computers & Geosciences* 32, no. 10: 1758–1768.

Toze, S., E. Bekele, D. Page, J. Sidhu, and M. Shackleton. 2010. Use of static quantitative microbial risk assessment to determine pathogen risks in an unconfined carbonate aquifer used for managed aquifer recharge. *Water Research* 44, no. 4: 1038–1049.

Tuller, M., and D. Or. 2005. Water retention and characteristic curve. In *Encyclopedia of Soils in the Environment*, ed. D. Hillel, 278–289. Oxford, UK: Elsevier.

Tyler, S.W., J.S. Selker, M.B. Hausner, C.E. Hatch, T. Torgersen, C.E. Thodal, and S.G. Schladow. 2009. Environmental temperature sensing using Raman spectra DTS fiber-optic methods. *Water Resources Research* 45: 1–11.

van de Giesen, N., S.C. Steele-Dunne, J. Jansen, O. Hoes, M.B. Hausner, S. Tyler, and J. Selker. 2012. Double-ended calibration of fiber-optic Raman spectra distributed temperature sensing data. *Sensors* 12, no. 5: 5471–5485.

Van Der Kamp, G., and S. Bachu. 1987. *Use of Dimensional Analysis in the Study of Thermal Effects of Various Hydrogeological Regimes*, Vol. 47, 23–28. Washington, DC: American Geophysical Union.

van Genuchten, M.T. 1980. A closed-form equation for predicting the hydraulic conductivity of unsaturated Soils1. *Soil Science Society of America Journal* 44, no. 5: 892.

Wagner, V., T. Li, P. Bayer, C. Leven, P. Dietrich, and P. Blum. 2014. Thermal tracer testing in a sedimentary aquifer: Field experiment (Lauswiesen, Germany) and numerical simulation. *Hydrogeology Journal* 22, no. 1: 175–187.

Wang, M., and N. Pan. 2008. Predictions of effective physical properties of complex multiphase materials. *Materials Science and Engineering R: Reports* 63, no. 1: 1–30.

Westhoff, M.C., H.H.G. Savenije, W.M.J. Luxemburg, G.S. Stelling, N.C. van de Giesen, J.S. Selker, L. Pfister, and S. Uhlenbrook. 2007. A distributed stream temperature model using high resolution temperature observations. *Hydrology and Earth System Sciences* 11, no. 4: 1469–1480.

Zheng, C., M. Bianchi, and S.M. Gorelick. 2011. Lessons learned from 25 years of research. *Groundwater* 49, no. 5: 649–662.

Zheng, C., and P.P. Wang. 1999. MT3DMS: A modular three-dimensional multispecies transport model for simulation of advection, dispersion, and chemical reactions of contaminants in groundwater systems; documentation and user's guide. Technical Report Contract Report SERDP-99-1. Vicksburg, Mississippi: U.S. Army Engineer Research and Development Center.

Authors' Note: The authors do not have any conflicts of interest or financial disclosures to report.